Pyroclastic flow deposits from a kimberlite eruption: The Orapa South Crater, Botswana

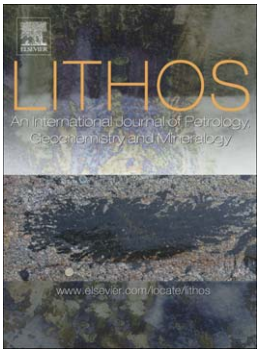

Pyroclastic flow deposits from a kimberlite eruption: The Orapa South Crater, Botswana

T.M. Gernon, G. Fontana, M. Field, R.S.J. Sparks, R.J. Brown, C. Mac Niocaill

PII: S0024-4937(09)00152-2
DOI: doi: 10.1016/j.lithos.2009.04.016
Reference: LITHOS 1968

To appear in: *LITHOS*

Received date: 8 September 2008
Accepted date: 19 April 2009

Please cite this article as: Gernon, T.M., Fontana, G., Field, M., Sparks, R.S.J., Brown, R.J., Niocaill, C. Mac, Pyroclastic flow deposits from a kimberlite eruption: The Orapa South Crater, Botswana, *LITHOS* (2009), doi: 10.1016/j.lithos.2009.04.016

Pyroclastic flow deposits from a kimberlite eruption: the Orapa South Crater, Botswana

T. M. Gernon [a,b,*], G. Fontana [c] M. Field [a] R. S. J. Sparks [a] R. J. Brown [a,d] and C. Mac Niocaill [c]

[a] *Department of Earth Sciences, University of Bristol, Wills Memorial Building, Bristol BS8 1RJ, U.K.*

[b] *Department of Geology, Trinity College, Dublin 2, Ireland.*

[c] *Department of Earth Sciences, University of Oxford, Oxford OX1 3PR, U.K.*

[d] *Department of Earth and Environmental Sciences, Open University, Milton Keynes, MK7 6AA, U.K.*

Abstract

The Orapa Diamond Mine (Republic of Botswana) exposes a bi-lobate kimberlite pipe that erupted during the Late-Cretaceous epoch (∼93 Ma) through Archaean basement and volcano-sedimentary rocks of the Karoo Supergroup. Geological mapping of the crater zone of the South Pipe has revealed a 15–25 m thick in-situ kimberlite pyroclastic flow deposit. The pyroclastic deposit fills in the crater and completely drapes lower units, indicating that the parent flow originated from an adjacent kimberlite pipe. The unit comprises a basal coarse lithic concentration layer exhibiting imbricated clasts, which grades upwards into massive poorly sorted lapilli tuff. The tuff contains abundant sub-vertical degassing structures defined by lithic enrichment and depletion in fine-grained material. Degassing structures commonly emanate from blocks in the basal layer. The presence of degassing structures and a coarse basal layer distinguishes this deposit from pipe-filling massive volcaniclastic kimberlite, which is typically homogeneous in terms of texture and clast size over distances on the order of 100s metres. Studies of the thermal remnant magnetism in basalt clasts from the deposit, together with serpentine–diopside assemblages, indicate that it was emplaced at elevated temperatures on the order of 200–440°C, consistent with deposition from a pyroclastic flow. The lithofacies characteristics can be explained by the interaction of the pyroclastic flow with the complex topography of a pre-existing crater.

Key words: kimberlite, crater, pyroclastic flow, Orapa, fluidisation, degassing

* Corresponding author.
Email address: gernont@tcd.ie (T. M. Gernon).

Introduction

Kimberlites are ultrabasic igneous rocks emplaced as pipes and dykes into regions of stable cratonic crust (e.g. southern Africa, N.W.T. Canada and Siberia, Russia). Downward tapering kimberlite pipes are typically divided into a lower root zone, a central diatreme zone and an upper crater zone (Hawthorne, 1975; Clement, 1982; Clement and Skinner, 1985; Mitchell, 1986; Clement and Reid, 1989; Sparks et al., 2006). Kimberlite volcanoes are somewhat unique in that most of the deposits are preserved in the conduit. Unlike at most other volcanoes, extra-crater deposits are not commonly preserved at kimberlite volcanoes, due to protracted erosion in their cratonic settings. The recognition of primary pyroclastic deposits preserved in a potentially distal setting is unique and of great importance in trying to unravel the dynamics of kimberlite eruptions.

Due to the extensive erosion that occurs in cratonic regions, kimberlite craters are not commonly preserved. Exceptions include the Orapa (A/K1) kimberlite pipes, Botswana (Field et al., 1997), the Mwadui kimberlite pipe, Tanzania (Stiefenhofer and Farrow, 2004) and the Argyle (AK1) lamproite pipe, Western Australia (Boxer et al., 1989). These craters typically contain re-sedimented VK and crudely-layered pyroclastic units. The latter are envisaged by Boxer et al. (1989), Field et al. (1997) and Stiefenhofer and Farrow (2004) to have formed in-situ by sustained deposition from eruption columns. Sparks et al. (2006) present an emplacement model in which primary pyroclastic processes (i.e. pyroclastic fall and flow) are important throughout the life of a kimberlite eruption. These can produce both layered and massive deposits.

Leahy (1997) and Leckie et al. (1997) describe crater-facies tuff deposits from flat-lying crater deposits of the Fort à la Corne kimberlite field, Saskatchewan, Canada. Crystal-tuff and lapillistone units in this field are interpreted as pyroclastic fall deposits (Leahy, 1997; Leckie et al., 1997). Pyroclastic flow deposits have also been identified in the Fort à la Corne field, although there is still considerable debate as to whether these flows infilled an excavated crater (Scott-Smith et al., 1994; Field and Scott-Smith, 1999; Berryman et al., 2004) or whether some of these flows may have been deposited outside the vent in a sub-marine environment where they have been preserved (Kjarsgaard et al., 2006; Pittari et al., 2008). Pyroclastic flow deposits have been reported from the Orapa A/K1 kimberlite (Field et al., 1997; Gernon et al., 2009), and are interpreted to have derived from a neighbouring pipe in the Orapa cluster (Gernon, 2007; Gernon et al., 2008, 2009). A similar style of cross-contamination between kimberlite pipes has also been invoked for the Diavik Pipe (Moss et al., 2008) and Ekati Fox Pipe (Porritt et al., 2008), NWT Canada.

In this paper we describe an unusual 25 m thick pyroclastic unit in the Orapa

South kimberlite pipe that we interpret as a pyroclastic flow deposit. Thermal Remnant Magnetism (TRM) analysis of lithic clasts within the deposit indicate that it was emplaced at elevated temperatures and the geometry of the unit, geological mapping and stratigraphic relationships with other units in the pipe indicate that it must have been derived from an eruption at a neighbouring kimberlite pipe *after* the cessation of volcanic activity at the Orapa South Pipe. The novelty of this study is that we demonstrate how palaeomagnetic studies coupled with lithofacies analysis and geological mapping can successfully distinguish between pyroclastic deposits and mass-flow deposits within kimberlite craters (e.g. debris flow deposits): this is commonly difficult in volcaniclastic successions as both types of deposit can exhibit similar lithofacies and features (Duyverman and Roobol, 1981; Cas and Wright, 1987; Nocita, 1988; Best, 1989, 1992).

The discovery of a pyroclastic flow deposit within a kimberlite pipe, which have been recently described elsewhere (Moss et al., 2008; Porritt et al., 2008), places additional constraints on the dynamics of kimberlite eruptions and allows comparisons with the deposits of pyroclastic flows from other better understood types of volcanoes. The success of the approach outlined here should prompt re-examination of other kimberlite crater deposits. Additional merits of this study are the economic ramifications of the cross-contamination of one pipe by eruptions from a neighbouring pipe, because diamond grade commonly varies significantly from one pipe to another, even within the same kimberlite cluster. The ability to differentiate the provenance of pyroclastic units within a kimberlite pipe is critical for the long-term planning of mining operations.

Thermal Remnant Magnetism (TRM) analysis

Palaeomagnetic determinations of emplacement temperatures of volcanic deposits are based on the fact that lithic clasts incorporated into a pyroclastic deposit will originally have been magnetised in-situ prior to eruption and will thus possess a primary or natural remnant magnetisation (NRM) aligned with the Earth's field (during their formation). If the deposits are emplaced above ambient temperatures, the lithic clasts are heated during and after their incorporation into the deposit and then cool to an ambient temperature in their present position. During this heating, a portion of the original magnetisation with blocking temperatures (T_b) less than or equal to the emplacement temperature will be reset, and replaced or overprinted by a new partial thermoremnant magnetisation (pTRM). The original high-T_b magnetisation will exhibit random orientations from clast to clast because they have been moved during eruption and incorporation into the deposit. The reset low-T_b magnetisation will have the same orientation in each clast (parallel to the Earth's magnetic field direction at the time of cooling). Therefore, the emplacement

temperature (T_e) of the lithic clasts can be determined by progressive thermal demagnetisation of the magnetic components present within the clast. The estimate of T_e is the temperature above which the overprinted magnetisation is removed and the randomised high temperature magnetisation is uncovered (e.g. McClelland and Druitt, 1989; Bardot, 2000).

Geological setting

The Orapa kimberlite cluster, comprising approximately 60 pipes and dykes, is located in north-eastern Botswana, east of the Central Kalahari sub-basin (Fig. 1A). During the Late-Cretaceous epoch (∼93 Ma), kimberlites of the North and South Pipes at Orapa (A/K1; Fig. 1A) were erupted through deformed Archaean basement overlain by volcanic and sedimentary rocks of the Karoo Supergroup (Carney et al., 1994; Field et al., 1997). The pipes are located near the inferred contact between the Archaean Limpopo Belt and Zimbabwe Craton. The Limpopo Belt (3500–2500 Ma), hosting the kimberlites, consists of structurally complex metamorphic terranes composed of variable proportions of gneiss, granitoids and meta-sedimentary rocks. In the Orapa region, the Karoo Supergroup comprises mudstones, fluvial and aeolian sandstones and basaltic lavas, the latter of which are exposed at the current mining level, and constitute multiple amygdaloidal basaltic lavas. The South Pipe at Orapa exposes stratified crater-facies rocks that lie unconformably over massive pipe-filling VK in the older North Pipe (Field et al., 1997; Gernon et al., 2009). The latter deposits are generally well-mixed, with layering confined to the margins, and preliminary TRM studies suggest that it was emplaced at eruption temperatures of approximately 600°C. It is interpreted that the massive VK of the North Pipe was deposited during the waning phase of the eruption (Field et al., 1997; Sparks et al., 2006).

Methods

Detailed geological mapping of the Orapa South Pipe (Fig. 1B & C) focussed on recording the volcanic lithofacies and structure of the pipe, together with clast-size distribution and fabric studies. Geological data were plotted on basemaps, and elevation measurements were taken using a Garmin eTrex Global Positioning System (GPS). Representative degassing structures and their host matrices were sampled, and thin sections of the samples were analysed using an optical microscope and a HITACHI S–3500N Scanning Electron Microscope (SEM). When mapping bench exposures, high resolution scaled digital photographs were taken and a montage of images was compiled. Using pho-

tographs, ∼3500 lithic clasts were manually digitised in Adobe Illustrator. Lithic clast outlines in the degassing structures and their host matrices were analysed individually using the ImageJ package (NIH, 2006). This generated long- and short-axis measurements and the angle of long axes to the horizontal. Rose diagrams of lithic orientations were generated using the Stereonet program. For purposes of comparison, plots of fluidisation pipes were coloured semi-transparent grey and superimposed on black plots representing the host matrix. In this paper, we follow the terminology for pyroclastic rocks developed by Fisher (1961) and White and Houghton (2006). For example, "ash" is defined as particles ≤2 mm in diameter.

TRM analysis

A total of 42 basalt lithic clasts were collected from the basal breccia lithofacies. The sampling of the lithic clasts followed the methodology outlined by McClelland and Druitt (1989) and Bardot (2000). Rigid plastic plates were glued to the surface of in-situ clasts and the strike and dip of the plate was recorded. Magnetisation of the samples was measured using a 2G Enterprises cryogenic magnetometer. The samples were demagnetized using a furnace with a residual field <5nT, in steps of 20°C or 40°C, up to 590°C (initial step 40°C). The principal components of magnetisation were analysed using the SuperIAPD2000 programme written by T.H. Torsvik, incorporating the LINEFIND algorithm of Kent et al. (1983). Magnetic components were considered stable where they were defined by at least three points on vector end-point diagrams and had a maximum angular deviation (MAD) not exceeding 15°. Statistical analysis of the magnetisation components and directional data were evaluated using spherical statistical parameters of Fisher (1953). The mean of a sample of N directions is calculated by vector addition, where R is the resultant vector and D and I are the declination and inclination respectively. An estimate of the dispersion of a sample of N directions (i.e. from a single site) is the precision parameter, k (which approaches N for a tightly clustered set of directions). The 95% confidence limit for the calculated mean direction is expressed as an angular radius from the calculated mean direction (α_{95}), which is analogous to twice the estimated standard error of the mean in Gaussian statistics. The significance of groupings of vector components from a site is assessed using the test for randomness of Watson (1956).

The growth of a new magnetic phase during either the eruption or laboratory heating could produce a chemical remanent magnetisation (CRM), which may partly or completely replace the existing magnetisation. The reliability of the emplacement temperature estimates was tested by monitoring the variation of magnetic susceptibility with temperature to determine the Curie temperature (T_c) of the magnetic-mineral assemblage in the basalt samples. The

susceptibility should remain constant until the T_c of the magnetic-mineral assemblage (e.g. 580°C for magnetite) is reached, regardless of the emplacement temperature of the sample. The T_c of representative samples was determined by taking measurements of low-field susceptibility versus temperature, using a CS-2 attachment to a KLY-2 Kappabridge. Measurements of susceptibility were made every 15–20 s as the sample was heated from 40–700°C, and then as it cooled back to 40°C.

Field observations

The Orapa South Pipe (Fig. 1B & C) consists of a stratiform crater-fill sequence (Gernon et al., 2009). Benches in the upper part of the pipe expose a 15–25-m-high and 250-m-long section through the pyroclastic unit (Figs. 2 & 3). The unit changes in thickness from 15-m in the south, to approximately 25-m in the north (Fig. 2), and the thickness decreases considerably (to ∼10-m) across the North Pipe. The pyroclastic unit is directly underlain by matrix-supported basalt-rich breccia, containing several discontinuous lithic-clast rich beds. The breccia unit drapes the lower stratigraphy of the crater (Fig. 1C), and is interpreted to have been deposited from a catastrophic wall-rock failure in the South Crater, followed by debris avalanches associated with mass wasting of the north crater wall (Gernon et al., 2009). The pyroclastic unit is overlain by a competent stratiform pipe-wide deposit, comprising well-stratified medium to coarse-grained olivine sand. The assemblage of sedimentary structures including parallel laminations, reverse and normal grading, erosional channels, load casts and thin (∼5–10-cm) and widespread (∼100–200-m) pebble horizons suggest that it was rapidly deposited from dilute suspensions by a sheet-flood mechanism (Gernon et al., 2009). Provisional studies of the TRM in basalt clasts from this unit suggest emplacement temperatures on the order of ≤100°C, consistent with an origin as cold epiclastic flows. The studied pyroclastic unit can be divided into a basal massive lithic breccia and an upper massive lapilli tuff that comprises lithic-rich pipes and sheets (Figs. 2 & 3).

Massive lapilli tuff (MLT) lithofacies

This lithofacies consists of massive poorly-sorted medium–coarse lithic lapilli (∼10% area) and vesicular amoeboid ash and fine lapilli in a matrix of altered olivine crystal fragments (size range: 250 μm–2 mm) and trace quantities of garnet, chrome diopside and ilmenite crystals. In the matrix, there is little appreciable variation in grain-size, either vertically or with distance. Basalt dominates the lithic clast population, although mantle nodules, basement schists and gneisses occur rarely. Lithic clasts vary in diameter from 1 –

225 cm (Fig. 4a & b). Lithic clasts are scattered evenly throughout (Fig. 5). However, lithic clasts are generally larger towards the base, defining a crude grading (Fig. 3). Fabric studies (Fig. 6) show that lithic clast orientations vary from place to place. In most places there is a moderate to strong tendency for long axes in the plane of the bench exposure to plunge toward the south-west. The lithofacies hosts abundant sub-vertical lithic-rich pipes and sheets (described below). Pore space is filled with low birefringence serpentine and less commonly calcite with void-filling (grainstone) textures.

Lithic-rich pipes and sheets

The massive lapilli tuff hosts abundant well-developed sub-vertical structures enriched in lithic fragments (size range = 1 mm–53.5 cm) and large crystals (altered olivine macrocrysts; size range = 500 μm–6.6 mm), and almost devoid of the fine-medium grained crystals and minor lithic components that comprise the surrounding MLT matrix (see Gernon et al., 2008).

The structures are observed both in sections of drill core (Fig. 7A), and in bench exposures (Fig. 7B). Small (decimetre-scale) structures are vertical and sheet-like (Fig. 5), becoming narrower upward and occasionally exhibiting branching. They are abundant in the uppermost 5 m of the MLT lithofacies. Larger (metre-scale) structures commonly originate from the upper surfaces of large lithic boulders in the basal breccia lithofacies (described below). The larger-scale sub-vertical structures narrow upward, with no indication of shear. In most cases, they are straight-sided, though some structures show branching and bifurcation. In limited 3D view, they are irregular, and some appear to be sheet-like.

In both the small and large-scale structures, the matrix proportion (5–10%) is lower than that in the host massive lithofacies (55–60%), and the structures are therefore marginally better sorted. The structures lack internal layering, are clast supported, and contain angular to sub-rounded lithic clasts and crystals (Fig. 7B & C). Lithic clasts dominantly comprise basalt (90%) with associated pockets of basalt-derived pyroxene fragments (augite ± titanomagnetite), and heavily altered plagioclase observed in voids. Minor quantities of phlogopite, perovskite and chrome spinel have been recorded in thin section.

Within the structures, lithic fabrics defined as long axis orientations in the vertical plane are more variable than they are in their host matrices. The fabrics within structures vary from random to steeply plunging (Fig. 6). Bimodal fabric orientations are displayed within and around many of the structures (Fig. 6). Lithic clasts in structures exhibit a similar size range to the host with the exception of several large boulders in the latter (Figs. 4 & 6).

In all structures, the inter-clast space is filled with secondary calcite, zeolite

and a serpentine–diopside assemblage with void-filling textures. Calcite and zeolite are generally restricted to narrow (∼300 μm) regions adjacent to clasts, where they are probably related to the breakdown of plagioclase (Leichmann et al., 2003; Batchelor et al., 2008). Polished slabs (Fig. 7C) and thin sections (Fig. 7D) show that void-filling serpentine and radial aggregates of cryptocrystalline diopside microlites are associated with concentrations of large olivines. Components for the serpentine infill (Mg and Si) are released from the olivine structure to fill the voids locally between olivine crystals during serpentinisation (Stripp et al., 2006).

Basal massive lithic breccia lithofacies

This lithofacies constitutes a coarse matrix-supported breccia (70% matrix; 30% lithic clasts), comprising angular to sub-angular basalt clasts in a poorly sorted matrix similar to the MLT. This lithofacies is laterally discontinuous, ∼5–12 m thick, and occurs at the base of the unit (Fig. 8). The lithofacies characteristics (e.g. lithic clast size and fabric) do not change significantly with distance. Local thickness variations are typically associated with infilling of topographic irregularities at the base of the unit. Lithic clasts vary from 0.02 m to 3.6 m in diameter (Fig. 4c), with a mean size of 0.1–0.15 m. Lithic clasts tend to decrease in size vertically upwards, defining a weak to moderate grading (Fig. 3).

Lithic clasts exhibit a moderate to strong imbrication with the majority of long axes plunging toward the south-west (Fig. 8) in the plane of the section. The basal part of the lithofacies contains occasional basalt boulders with subhorizontal long axes and maximum dimensions of approximately 2 to 4 m. Subvertical lithic-rich pipes and sheets emanate from the sides and tops of these boulders (Figs. 6 & 8). The contact between the basal breccia and overlying massive lithofacies is gradational, typically occurring over 0.5 m, and is marked by a decrease in the size and abundance of basalt clasts (Fig. 8). In places, the upper surface of the breccia is hummocky and exhibits irregular concentrations of lithic clasts (Fig. 2B).

Lithofacies interpretation

On the basis of the very poor sorting, disorganized fabric, crude grading and presence of lithic-rich pipes and sheets, the unit most likely represents deposition by highly concentrated granular mass flows (Smith, 1986; Iverson and Vallance, 2001; Manville and White, 2003). The lithic-rich pipes and sheets are very coarse grained, fines-poor, internally massive and are interpreted as fluid escape structures (Walker, 1971; Wilson, 1980; Branney and Kokelaar, 2002;

Gernon et al., 2008). Although such structures are found mainly in pyroclastic flow deposits (Walker, 1971; Sparks et al., 1985; Freundt and Schmincke, 1986; Cas and Wright, 1987; Sparks et al., 1999), they are occasionally reported from cold, wet mass flow deposits (Duyverman and Roobol, 1981; Nocita, 1988; Best, 1989, 1992). The crude normal grading observed in these deposits can be explained by density-stratification in particulate flows suspended by either liquids in debris flows (Takahashi, 1981; Smith, 1986; Smith and Lowe, 1991; Iverson and Vallance, 2001; Manville and White, 2003) or gases in pyroclastic flows (Walker, 1971; Sparks et al., 1973; Sparks and Walker, 1973; Sparks, 1976; Druitt and Sparks, 1982; Freundt and Schmincke, 1985b; Branney and Kokelaar, 2002).

Distinguishing between these two modes of deposition is in fact rather difficult, mainly since we have no concept of what distal, primary kimberlite pyroclastic flow deposits would look like. Other kimberlite occurrences interpreted as pyroclastic flow deposits have been sorted in a deep water column (Moss et al., 2008), or have been deposited by column collapse, and consequently transported over negligible distances (Porritt et al., 2008).

One strong line of evidence is provided by the diopside–serpentine assemblage filling voids, which is estimated to form in the range 370–250°C (Stripp et al., 2006). Assuming the assemblage was formed during hydrothermal metamorphism as the pyroclastic deposit cooled (Berg, 1989; Stripp et al., 2006), this suggests higher temperatures (≥250°C) during emplacement (Gernon et al., 2008), therefore favouring deposition by a hot pyroclastic flow. In order to test this hypothesis, thermal remnant magnetism was applied to basalt clasts from the basal massive lithic breccia.

TRM analysis of basalt clasts

Well-defined emplacement temperatures can be determined from basalt clasts in which a two-component magnetisation is identified, following progressive thermal demagnetisation. A total of 23 samples taken from the breccia displayed a two-component magnetisation (Type-1 behaviour; Fig. 9a). Figure 9a shows that all points from 0–240°C in this sample lie on a well-fitted line (MAD = 2.9) with a direction of D = 342.3°, I = - 54.9°, which is similar to the local Cretaceous field direction of D = 350°, I = - 69° (Hargraves and On-Stott, 1980). All points from 280–590°C lie on a high-temperature line (MAD = 10.0) with a direction of D = 245.1°, I = -65.9°, statistically different from the low-temperature component and Cretaceous field direction. An emplacement temperature (T_e) estimate uses the temperature range between the last point on the low-temperature line and the second point on the high-temperature line, in this case T_e = 240–280°C. The low-temperature components in Type-

1 clasts are well-grouped at the 95% confidence level (α_{95} = 12.2°; Fig. 9c) which indicates that they represent the thermal overprints acquired during emplacement at elevated temperatures. The high-temperature components are scattered (α_{95} = 30.4; Fig. 9d) and represent the original magnetisations of the clasts randomized during their transport and deposition. The mean direction of low-temperature components (D = 330°, I= -43.9°) is close to, but statistically different, from the Cretaceous field direction in the Orapa area (Fig. 9c). These variations could result from movement of the basalt clasts within the deposit during compaction. An alternative explanation is that slumping of the deposit may have rotated the clasts, and this would be independent of the dominant imbrication orientation (long axes plunging toward the south-west; see Fig. 8).

Other behaviour types prevent a well-defined determination of emplacement temperature but provide important constraints on T_e estimates within the deposit. In 14 samples, the natural magnetic-grain size distribution is extremely restricted and no grains with low-T_bs are present. This is defined as Type-2 behaviour, illustrated in Fig. 9b. In this sample, little or no demagnetisation occurs in heating steps below 480°C, after which 90% of the magnetisation is removed. No thermal overprint would be recorded in these clasts if heated to temperatures less than the minimum T_bs. The single-components in these samples are poorly grouped at the 95% confidence level (α_{95} = 75.2°), and indistinguishable from a random grouping. Therefore the clasts are considered to have been emplaced at temperatures less than the minimum T_bs. These samples provide maximum emplacement temperatures for the deposit (e.g. <480°C for the sample in Fig. 9b). The remaining 5 samples display single-component magnetisations with a random direction, but possess a broad spectra of blocking temperatures that should record a thermal overprint if emplaced at elevated temperatures. These are interpreted as clasts that may have been emplaced at >590°C, but have moved following cooling, or alternatively as clasts that were emplaced at ambient temperatures. Due to this ambiguity in possible interpretations, they are not included in the emplacement temperature study.

The reliability of the emplacement temperature estimates was tested by taking measurements of low-field susceptibility versus temperature in representative basalt samples. In these samples the susceptibility remained constant until dropping to zero at temperatures between 500–600°C, indicating that magnetite is the dominant magnetic-mineral assemblage. Similar behaviour is observed between clasts that provide different emplacement temperature results, supporting the reliability of the emplacement temperature estimates. The emplacement temperature estimates of individual lithic clasts are illustrated in figure 9e. The range of emplacement temperatures obtained from a two-component clasts lie in the range of 200–440°C. Upper limits of emplacement temperature of 510°C are provided from lithic clasts exhibiting Type-2 behaviour.

Interpretation

The mass flow deposit forms part of a stratified volcaniclastic sequence across the entire pipe (Fig. 1). It overlies a clast-supported lithic breccia unit (Gernon et al., 2009), which itself overlies lower vent-fill pyroclastic deposits. The TRM results described above rule out deposition from a cold, wet debris flow and are more consistent with deposition from a hot pyroclastic flow. Stratigraphic constraints indicate that the deposit is derived from another pipe. Since the South Crater post-dates emplacement of the North Pipe (Field et al., 1997), we infer that the pyroclastic flow originated from an adjacent pipe complex — the Orapa South Pipe simply collected and preserved the pyroclastic flow deposit. At least seven kimberlite pipes have been discovered within a 10 km radius of A/K1, mainly to the south and the east.

There are many examples of pyroclastic flows flowing many tens of kilometres from caldera depressions or from isolated vents (Wilson, 1985; Wilson and Walker, 1985; Wilson et al., 1995; Cas and Wright, 1987; Buesch, 1993). In explosive volcanic eruptions two main factors control pyroclastic flow run-out and flow energetics, one being the height of the volcanic edifice and the other being the height of the collapsing eruption column (Sparks and Wilson, 1976). The latter factor becomes dominant in high intensity eruptions and in cases where there is no edifice. The Laacher See Volcano (Germany), which comprises a maar-type crater, produced pyroclastic flows that travelled at least 10 km from the source (Freundt and Schmincke, 1985a, 1986).

Discussion

We have documented a sheet-form pyroclastic unit that comprises a basal imbricated lithic breccia that grades into a poorly-sorted massive lapilli tuff that hosts abundant fines-poor vertical structures, which we attribute to gas escape. These features are characteristic of pyroclastic flow deposits formed in basaltic and silicic eruptions (Walker, 1971; Sparks, 1976; Cas and Wright, 1987; Branney and Kokelaar, 2002). There seems little doubt from the TRM results that the deposit was emplaced at elevated temperatures on the order of 200–440°C. This temperature range is consistent with emplacement temperatures determined for pyroclastic flow deposits at other volcanoes, such as Santorini, Greece (250–$\geq$580°C; McClelland and Druitt, 1989), Vesuvius, Italy (180–400°C; Kent et al., 1981; Cioni et al., 2004), and Lascar, Chile (200–300°C; Thomas, 1993; Gardeweg et al., 1998).

Deposition of the basal lithofacies

The basal lithic concentration horizon is interpreted as a lithic lag breccia deposited rapidly upon deceleration of a pyroclastic flow. Such breccias are typically found at the base of ignimbrites (Walker, 1985), and can form in a variety of environments from proximal to distal. Commonly they form within 0.5 to 20 km from the site of eruptive column collapse (Wright and Walker, 1977, 1981; Walker, 1985; Druitt and Sparks, 1982). Lithic lag breccias are commonly found in proximal regions, where they can deposit both inside and outside the inflation-deflation zone of the collapsing fountain. However, they can also form in medial to distal regions where flows interact with topography. In medial to distal regions, fast-moving pyroclastic flows in highly irregular topography can erode talus, entrain coarse lapilli and blocks and deposit them locally, as documented in studies such as Freundt and Schmincke (1985b, 1986), Roobol et al. (1987), Buesch (1992), Cole et al. (1993), Sparks et al. (1997), Macías et al. (1998), Calder et al. (2000) and Brown and Branney (2004). A pre-existing crater is an environment where a pyroclastic flow can encounter large local accelerations and decelerations, hydraulic jumps and mixing with ambient air as the flow moves over the crater rim (Fig. 10A). At Orapa, the lag breccias are attributed to the interaction of the pyroclastic flow with the local topography as it entered the Orapa South Crater, entraining locally derived basalt clasts that would have characterised loose slope talus and walls of the pre-existing crater (Fig. 10A). This environment favours the formation of local lag breccias, with blocks and fluid escape structures. Alternatively, some of the basalt clasts might have been entrained from source. A moderate to strong imbrication developed within the basal layer (see Fig. 8) suggests that the flow entered the crater from the south to south-west. However, there are no constraints on the local palaeo-topography outside of the Orapa A/K1 Pipe during emplacement and the deposit cannot yet be linked to a specific pipe in the Orapa cluster.

Formation of the degassing structures

The degassing structures (see Gernon et al., 2008) are hosted by massive lapilli tuff, and are comparable to elutriation pipes described from ignimbrites (Walker, 1971; Sparks et al., 1985; Branney and Kokelaar, 2002). The structures are unsheared and therefore probably formed after deposition (Fig. 10B). Observations show that the structures originally contained little fine ash matrix, with the pore space infilled by up to 25% secondary calcite, zeolite, serpentine and diopside. The inferred high porosity and paucity of fine particles can be explained by the gas-driven elutriation of fines (Walker, 1971).

Gas may have been sourced from volatile exsolution (c.f. Sparks et al., 1999), attrition between particles (c.f. Druitt, 1995; Branney and Kokelaar, 2002), boiling of groundwater (c.f. Sparks, 1978; Gurioli et al., 2002), or entrainment of air (c.f. Sparks et al., 1985) as the pyroclastic flow entered the South Crater. Air may also have been entrained during initial column formation, during fountaining and during transport across the ground prior to entering the crater. The localisation of degassing structures over blocks is explained by blocks acting as sites for gas accumulation and channelling (Branney and Kokelaar, 2002). Such obstacle-induced bubbling and segregation by bubbles has been documented in gas-fluidisation experiments (Duursma et al., 1994; Gilbertson and Eames, 2001). Within the degassing structures, vertical clast orientations can be explained by the preferred alignment of platy particles parallel to the upward gas streams (Massey, 1998; Streeter et al., 1998). As the gas flow-rate dropped and the pyroclasts within the pipes became de-fluidised, some particles rotated to attain a state of mechanical stability. Rotation could have occurred in two opposing directions depending on shape, accounting for the bimodal clast orientations observed.

Comparison with typical massive volcaniclastic vent-fill

The fact that these pyroclastic flow deposits form part of a stratiform crater sequence comprising sedimentary units (Gernon et al., 2009) distinguishes them from typical pipe-filling massive volcaniclastic kimberlite (MVK), such as, for example, that of the Venetia K1 Pipe, South Africa (Gernon et al., this volume). In addition, the Orapa deposits are relatively thin, crudely graded, and comprise a laterally extensive coarse basal lithofacies, which are generally not characteristic of MVK. On the contrary, MVK is typically homogeneous in terms of texture and clast size over distances on the order of 100s metres (see Figs. 2 & 3, Gernon et al., this volume). Laterally continuous, sub-horizontal layering is generally not observed in MVK. Further, degassing structures are typically isolated in MVK (Gernon et al., 2008, this volume), as opposed to being concentrated along a particular stratigraphic level, as is observed in these deposits (Fig. 6).

Insights into kimberlite eruptions

The discovery of this pyroclastic flow deposit is important because it indicates that kimberlite volcanoes are not exactly comparable to small basaltic volcanoes. The evidence presented here suggests that kimberlite eruptions are capable of producing sustained (fountaining) eruption columns and thick pyroclastic flow deposits. The evidence also shows that pyroclastic flows gen-

erated in kimberlite eruptions can involve significant transport away from source (probably 5–10 km). This suggests that kimberlite volcanoes are capable of producing violent Strombolian and perhaps (sub-) Plinian eruptions (see Sparks et al., 2006). Basaltic eruptions that are similar in terms of explosive intensity might include the 1886 Plinian eruption of Tarawera, the early phases of the 1943 Parícutin eruption (which were moderate to high intensity and comparable to the rates proposed in Sparks et al., 2006) and the 1975 sub-Plinian Tolbachik eruption, which excavated a conduit at least 2 km deep (Doubik and Hill, 1999).

Conclusions

We have documented kimberlite pyroclastic flow deposits with associated degassing structures, emplaced at high temperatures of 200–440°C as constrained by TRM studies of basalt lithic clasts and serpentine–diopside assemblages. The pyroclastic flow deposit formed a continuous sheet across the Orapa South Pipe, indicating that the flow originated from another kimberlite vent and was emplaced into the Orapa South Crater. The deposit also provides evidence that kimberlite eruptions can produce sustained hot pyroclastic flows capable of travelling kilometres away from source. This type of cross-contamination within kimberlite clusters has major implications for diamond exploration and the economic evaluation of pipes. Recognition of this specific kimberlite deposit requires an eruption process capable of: (1) comprehensive fragmentation, (2) production of gas-charged mass flows, and (3) significant transport away from the vent. The lithofacies of the pyroclastic flow deposit are typical of an environment where the flow encounters complex topography.

Acknowledgements

This research was supported by a De Beers Group Services UK studentship. De Beers and the Debswana Diamond Company are thanked for permission to publish geological data. We acknowledge the hospitality of Debswana and input of geologists at Orapa Mine, particularly P. Kesebonye, P. Khutjwe, A. Doorgapershad and E. Seane. Thanks go to Stuart Kearns for his assistance with the SEM. We acknowledge helpful discussions with M.A. Gilbertson, T.K. Hincks and M. Branney, and thank J.K. Russell, G.A. Valentine, C.J.N. Wilson, R.A.F. Cas, V. Lorenz and J.D.L. White for their constructive reviews of an earlier version of this paper. Two anonymous reviewers provided helpful comments, and V. Lorenz is thanked for providing editorial support.

References

Bardot, L., 2000. Emplacement temperature determinations of proximal pyroclastic deposits on Santorini, Greece, and their implications. Bulletin of Volcanology, 61, 450–467.

Batchelor, R. A., Prave, A. R., Oliver, G. J. H., Raeburn, A. S., 2008. Petrogenesis of albite-rich mid- to late Proterozoic tephra-fall deposits ('brown beds'). Geological Magazine, 145 (6), 858–867, Doi: 10.1017/S0016756808004962.

Berg, G. W., 1989. The significance of brucite in Southern African kimberlites. In: Ross, J. (Ed.), Kimberlite and Related Rocks, Volume 2; Their Mantle/Crust Setting. Diamonds and Diamond Exploration. Vol. 14. Blackwell Scientific, Victoria, Australia, pp. 282–296.

Berryman, A. K., Scott-Smith, B. H., Jellicoe, B. C., 2004. Geology and diamond distribution of the 140/141 kimberlite, Fort à la Corne, central Saskatchewan, Canada. Lithos, 76, 99–114.

Best, J. L., 1989. Fluidization pipes in volcaniclastic mass flows, Volcan Hudson, Southern Chile. Terra Nova, 1, 203–208.

Best, J. L., 1992. Sedimentology and event timing of a catastrophic volcaniclastic mass flow, Volcan Hudson, Southern Chile. Bulletin of Volcanology, 54, 299–318.

Boxer, G. L., Lorenz, V., Smith, C. B., 1989. The geology and volcanology of the Argyle (AK1) lamproite diatreme, Western Australia. In: Ross, J. (Ed.), Kimberlites and related rocks: Their composition, occurrence, origin and emplacement. Vol. 1. Geological Society of Australia, Sydney (Blackwell Scientific Publications, Oxford), pp. 140–152.

Branney, M. J., Kokelaar, P., 2002. Pyroclastic density currents and the sedimentation of ignimbrites. No. 27. Geological Society, London, Special Publications.

Brown, R. J., Branney, M. J., 2004. Bypassing and diachronous deposition from density currents: Evidence from a giant regressive bed form in the Poris ignimbrite, Tenerife, Canary Islands. Geology, 32 (5), 445–448.

Buesch, D. C., 1992. Incorporation and redistribution of locally derived lithic fragments within a pyroclastic flow. Geological Society of America Bulletin, 104, 1193–1207.

Buesch, D. C., 1993. Feldspar geochemistry of four Miocene ignimbrites in southeastern California and western Arizona. In: Sherrod, D. R., Nielson, J. E. (Eds.), Tertiary stratigraphy of highly extended terranes, California, Arizona, and Nevada. Vol. 2053. U. S. Geological Survey, pp. 55–85.

Calder, E. S., Sparks, R. S. J., Gardeweg, M. C., 2000. Erosion, transport and segregation of pumice and lithic clasts in pyroclastic flows inferred from ignimbrite at Lascar Volcano, Chile. Journal of Volcanology and Geothermal Research, 104, 201–235.

Carney, J. N., Aldiss, D. T., Lock, N. P., 1994. The Geology of Botswana. Geological Survey Department of Botswana.

572 Cas, R. A. F., Wright, J. V., 1987. Volcanic Successions: Modern and Ancient.
573 Allen and Unwin.
574 Cioni, R. L., Gurioli, L., Lanza, R., Zanella, E., 2004. Temperatures of the
575 A.D. 79 pyroclastic density current deposits (Vesuvius, Italy). Journal of
576 Geophysical Research, 109, Doi: 10.1029/2002JB002251.
577 Clement, C. R., 1982. A comparitive geological study of some major kimberlite
578 pipes in northern Cape and Orange Free State. Ph.D. thesis, University of
579 Cape Town.
580 Clement, C. R., Reid, A. M., 1989. The origin of kimberlite pipes: an interpre-
581 tation based on the synthesis of geological features displayed by southern
582 African occurrences. In: Ross, J., Jaques, A. L., Fergusan, J., Green, D. H.,
583 O'Reilly, S. Y., Danchin, R. V., Janse, A. J. A. (Eds.), Kimberlites and
584 related rocks. Vol. 14. Geological Society of Australia, Sydney, pp. 632–646.
585 Clement, C. R., Skinner, E. M. W., 1985. A textural-genetic classification of
586 kimberlites. South African Journal of Geology, 88 (2), 403–409.
587 Cole, P. D., Guest, J. E., Duncan, A. M., 1993. The emplacement of intermedi-
588 ate volume ignimbrites: A case study from Roccamonfina Volcano, Southern
589 Italy. Bulletin of Volcanology, 55, 467–480.
590 Doubik, P., Hill, B. E., 1999. Magmatic and hydromagmatic conduit devel-
591 opment during the 1975 Tolbachik Eruption, Kamchatka, with implications
592 for hazards assessment at Yucca Mountain, NV. Journal of Volcanology and
593 Geothermal Research, 91 (1), 43–64.
594 Druitt, T. H., 1995. Settling behaviour of concentrated dispersions and some
595 volcanological applications. Journal of Volcanology and Geothermal Re-
596 search, 65, 27–39.
597 Druitt, T. H., Sparks, R. S. J., 1982. A proximal ignimbrite breccia facies
598 on Santorini Volcano, Greece. Journal of Volcanology and Geothermal Re-
599 search, 13, 147–171.
600 Duursma, G. R., Ockendon, J. R., Hogan, S. J., 1994. Obstacle-Induced Voids
601 in Two-Dimensional Gas Fluidized Beds. Chemical Engineering Science,
602 49 (2), 233–244.
603 Duyverman, H. J., Roobol, M. J., 1981. Gas pipes in Eocambrian volcanic
604 breccias. Geological Magazine, 118 (3), 265–270.
605 Field, M., Gibson, J. G., Wilkes, T. A., Gababotse, J., Khutjwe, P., 1997. The
606 geology of the Orapa A/K1 kimberlite Botswana: further insights into the
607 emplacement of kimberlite pipes. Russian Geology and Geophysics, 38 (1),
608 24–39.
609 Field, M., Scott-Smith, B. H., 1999. Contrasting geology and near-surface
610 emplacement of kimberlite pipes in southern Africa and Canada. Lithos,
611 76, 214–237.
612 Fisher, R. A., 1953. Dispersion on a sphere. Proceedings of the Royal Astro-
613 nomical Society, London, A217, 295–305.
614 Fisher, R. V., 1961. Proposed classification of volcaniclastic sediments and
615 rocks. Geological Society of America Bulletin, 72, 1409–1414.
616 Freundt, A., Schmincke, H. U., 1985a. Hierarchy of facies of pyroclastic flow

deposits generated by Laacher See-type eruptions. Geology, 13, 278–281.
Freundt, A., Schmincke, H. U., 1985b. Lithic-enriched segregation bodies in pyroclastic flow deposits in Laacher See Volcano, (East Eifel, Germany). Journal of Volcanology and Geothermal Research, 25, 193–224.
Freundt, A., Schmincke, H. U., 1986. Emplacement of small-volume pyroclastic flows at Laacher See (East Eifel, Germany). Bulletin of Volcanology, 48, 39–59.
Gardeweg, M. C., Sparks, R. S. J., Matthews, S. J., 1998. Evolution of Lascar Volcano, Northern Chile. Journal of the Geological Society, London, 155, 89–104.
Gernon, T. M., 2007. Fluidisation and emplacement processes in kimberlite eruptions. Ph.D. thesis, University of Bristol.
Gernon, T. M., Field, M., Sparks, R. S. J., 2009. Depositional processes in a kimberlite crater: the Upper Cretaceous Orapa South Pipe (Botswana). Sedimentology, 56 (2), 623–643, Doi: 10.1111/j.1365-3091.2008.00989.x.
Gernon, T. M., Gilbertson, M. A., Sparks, R. S. J., Field, M., this volume. The role of gas-fluidisation in the formation of massive volcaniclastic kimberlite. Lithos.
Gernon, T. M., Sparks, R. S. J., Field, M., 2008. Degassing structures in volcaniclastic kimberlite: examples from southern African kimberlite pipes. Journal of Volcanology and Geothermal Research, 174 (1-3), 186–194, Doi: 10.1016/j.jvolgeores.2007.12.035.
Gilbertson, M. A., Eames, I., 2001. Segregation patterns in gas-fluidized systems. Journal of Fluid Mechanics, 433, 347–356.
Gurioli, L., Cioni, R., Sbrana, A., Zanella, E., 2002. Transport and deposition of pyroclastic density currents over an inhabited area: the deposits of the AD 79 eruption of Vesuvius at Herculaneum, Italy. Sedimentology, 49, 929–953.
Hargraves, R. B., On-Stott, T. C., 1980. Palaeomagnetic results from some South African kimberlites, and their tectonic significance. Journal of Geophysical Research, 85 (B7), 3587–3596.
Hawthorne, J. B., 1975. Model of a kimberlite pipe. Physics and Chemistry of the Earth, 9, 1–15.
Iverson, R. M., Vallance, J. W., 2001. New views of granular mass flows. Geology, 29 (2), 115–118.
Kent, D. V., Ninkovich, D., Pescatore, T., Sparks, R. S. J., 1981. Palaeomagnetic determination of emplacement temperature of Vesuvius AD 79 pyroclastic deposits. Nature, 290, 393–396.
Kent, J. T., Briden, J. C., Mardia, K. V., 1983. Linear and planar structure in ordered multivariate data as applied to progressive demagnetization of palaeomagnetic remanence. Geophysical Journal of the Royal Astronomical Society, 75, 593–621.
Kjarsgaard, B., Harvey, S., Zonneveld, J., Heaman, L., White, D., MacNeil, D., 2006. Volcanic stratigraphy, eruptive sequences and emplacement of the 140/141 kimberlite, Fort à la Corne field, Saskatchewan. In: Kimberlite Emplacement Workshop, Saskatoon, Canada.

Leahy, K., 1997. Discrimination of reworked pyroclastics from primary tephra-fall tuffs: a case study using kimberlites of Fort á la Corne, Saskatchewan, Canada. Bulletin of Volcanology, 59, 65–71.

Leckie, D. A., Kjarsgaard, B. A., Bloch, J., McIntyre, D., McNeil, D., Stasiuk, L., Heaman, L., 1997. Emplacement and reworking of Cretaceous, diamond-bearing, crater facies kimberlite of central Saskatchewan, Canada. Geological Society of America Bulletin, 109 (8), 1000–1020.

Leichmann, J., Broska, I., Zachovalová, K., 2003. Low-grade metamorphic alteration of feldspar minerals: a CL study. Terra Nova, 15 (2), 104–108.

Macías, J. L., Espíndola, J. M., Bursik, M., Sheridan, M. F., 1998. Development of lithic-breccias in the 1982 pyroclastic flow deposits of El Chichón Volcano, Mexico. Journal of Volcanology and Geothermal Research, 83, 173–196.

Manville, V., White, J. D. L., 2003. Incipient granular mass flows at the base of sediment-laden floods, and the roles of flow competence and flow capacity in the deposition of stratified bouldery sands. Sedimentary Geology, 155, 157–173.

Massey, B., 1998. Mechanics of Fluids, 7th Edition. Spon Press.

McClelland, E. A., Druitt, T. H., 1989. Palaeomagnetic estimates of emplacement temperatures of pyroclastic deposits on Santorini, Greece. Bulletin of Volcanology, 51, 16–27.

Mitchell, R. H., 1986. Kimberlites: Mineralogy, Geochemistry, and Petrology. Plenum Press.

Moss, S., Russell, J. K., Andrews, G. D. M., 2008. Progressive infilling of a kimberlite pipe at Diavik, Northwest Territories, Canada: Insights from volcanic facies architecture, textures, and granulometry. Journal of Volcanology and Geothermal Research, 174 (1-3), 103–116.

NIH, 2006. ImageJ software package, U.S. National Institute of Health. URL `http://rsb.info.nih.gov/ij/download.html`

Nocita, B. W., 1988. Soft-sediment deformation (fluid escape) features in a coarse-grained pyroclastic-surge deposit, north-central New Mexico. Sedimentology, 35, 275–285.

Pittari, A., Cas, R. A. F., Lefebvre, N., Robey, J., Kurszlaukis, S., Webb, K., 2008. Eruption processes and facies architecture of the Orion Central kimberlite volcanic complex, Fort à la Corne, Saskatchewan; kimberlite mass flow deposits in a sedimentary basin. Journal of Volcanology and Geothermal Research, 174, 152–170.

Porritt, L. A., Cas, R. A. F., Crawford, B. B., 2008. In-vent column collapse as an alternative model for massive volcaniclastic kimberlite emplacement: An example from the Fox kimberlite, Ekati Diamond Mine, NWT, Canada. Journal of Volcanology and Geothermal Research, 174 (1-3), 90–102.

Roobol, M. J., Smith, A. L., Wright, J. V., 1987. Lithic breccias in pyroclastic flow deposits on St. Kitts, West Indies. Bulletin of Volcanology, 49 (694-707).

Scott-Smith, B. H., Orr, R. G., Robertshaw, P., Avery, R. W., 1994. Geology

of the Fort à la Corne kimberlites, Saskatchewan. In: Jambor, J. L. (Ed.), Proc. 16th CIM District 6 AGM, Vancouver, Canada. pp. 19–24.

Smith, G. A., 1986. Coarse-grained nonmarine volcaniclastic sediment: Terminology and depositional process. Geological Society of America Bulletin, 97, 1–10.

Smith, G. A., Lowe, D. R., 1991. Lahars: volcano-hydrologic events and deposition in the debris flow—hyperconcentrated flow continuum. In: Sedimentation in volcanic settings. No. 45. Society for Sedimentary Geology, pp. 59–70.

Sparks, R. S. J., 1976. Grain-size variations in ignimbrites and implications for the transport of pyroclastic flows. Sedimentology, 23, 147–188.

Sparks, R. S. J., 1978. Gas release rates from pyroclastic flows: an assessment of the role of fluidisation in their emplacement. Bulletin of Volcanology, 41, 1–9.

Sparks, R. S. J., Baker, L., Brown, R., Field, M., Schumacher, J., Stripp, G., Walters, A., 2006. Dynamical constraints on kimberlite volcanism. Journal of Volcanology and Geothermal Research, 155, 18–48, Doi: 10.1016/j.jvolgeores.2006.02.010.

Sparks, R. S. J., Francis, P. W., Hamer, R. D., Pankhurst, R. J., O'Callaghan, L. O., Thorpe, R. S., Page, R., 1985. Ignimbrites of the Cerro Galan Caldera, NW Argentina. Journal of Volcanology and Geothermal Research, 24, 205–248.

Sparks, R. S. J., Gardeweg, M. C., Calder, E. S., Matthews, S. J., 1997. Erosion by pyroclastic flows on Lascar Volcano, Chile. Bulletin of Volcanology, 58, 557–565.

Sparks, R. S. J., Self, S., Walker, G. P. L., 1973. Products of ignimbrite eruptions. Geology, 1 (3), 115–118.

Sparks, R. S. J., Tait, S. R., Yanev, Y., 1999. Dense welding caused by volatile resorption. Journal of the Geological Society, London, 156, 217–225.

Sparks, R. S. J., Walker, G. P. L., 1973. The ground surge deposit; A third type of pyroclastic rock. Nature, 241, 62–64.

Sparks, R. S. J., Wilson, L., 1976. A model for the formation of ignimbrite by gravitational column collapse. Journal of the Geological Society, London, 132, 441–451.

Stiefenhofer, J., Farrow, D. J., 2004. Geology of the Mwadui kimberlite, Shinyanga district, Tanzania. Lithos, 76, 139–160.

Streeter, V. L., Wylie, E. B., Bedford, K. W., 1998. Fluid Mechanics, 9th Edition. McGraw-Hill.

Stripp, G. R., Field, M., Schumacher, J. C., Sparks, R. S. J., Cressey, G., 2006. Post emplacement serpentinization and related hydrothermal metamorphism in a kimberlite from Venetia, South Africa. Journal of Metamorphic Geology, 24, 515–534.

Takahashi, T., 1981. Debris flow. Annual Review of Fluid Mechanics, 13, 57–77.

Thomas, R. M. E., 1993. Determination of the emplacement temperature of

pyroclastic deposits by theoretical and palaeomagnetic methods. Ph.D. thesis, University of Bristol.

Walker, G. P. L., 1971. Grain-size characteristics of pyroclastic deposits. Journal of Geology, 79, 696–714.

Walker, G. P. L., 1985. Origin of coarse lithic breccias near ignimbrite source vents. Journal of Volcanology and Geothermal Research, 25, 157–171.

Watson, G. S., 1956. A test for randomness of directions. Monthly Notices, Royal Astronomical Society, Geophysical Supplement, 7, 160–161.

White, J. D. L., Houghton, B. F., 2006. Primary volcaniclastic rocks. Geology, 34 (8), 677–680.

Wilson, C. J. N., 1980. The role of fluidisation in the emplacement of pyroclastic flows: an experimental approach. Journal of Volcanology and Geothermal Research, 8, 231–249.

Wilson, C. J. N., 1985. The Taupo Eruption, New Zealand II. The Taupo Ignimbrite. Philosophical Transactions of the Royal Society of London. Series A, Mathematical and Physical Sciences, 314 (1529), 229–310.

Wilson, C. J. N., Houghton, B. F., Kamp, P. J., McWilliams, M. O., 1995. An exceptionally widespread ignimbrite with implications for pyroclastic flow emplacement. Nature, 378, 605–607.

Wilson, C. J. N., Walker, G. P. L., 1985. The Taupo Eruption, New Zealand I. General Aspects The Taupo Eruption, New Zealand I. General Aspects. Philosophical Transactions of the Royal Society of London. Series A, Mathematical and Physical Sciences, 314 (1529), 199–228.

Wright, J. V., Walker, G. P. L., 1977. The ignimbrite source problem: significance of a co-ignimbrite lag-fall deposit. Geology, 5, 729–732.

Wright, J. V., Walker, G. P. L., 1981. Eruption, transport and deposition of ignimbrite: a case study from Mexico. Journal of Volcanology and Geothermal Research, 9, 111–131.

Figure captions

Figure 1: (A) Map of Botswana showing the regional context of the Orapa A/K1 body; (B) Summary geological map of the Orapa South Crater (modified after Gernon et al., 2009); (C) Schematic cross-section a—b (refer to B). Note that drill-core logs were produced at an early stage and the pit has since been deepened by mining to the recent (2006) configuration shown in the section. Vertical exaggeration = 2.4.

Figure 2: (A) Photomontage of the Orapa South Crater (looking southeast), showing the distribution and stratigraphic context of the pyroclastic flow deposits. The wall-rock comprises Stormberg Formation basalts and Ntane Formation sandstones, the latter of which crop out as a septum between the North Pipe and the South Crater; (B) detail from (A) showing the nature of the transition between the basal massive breccia lithofacies and upper massive lapilli tuff (looking south). Note the irregular lower contact and the hummocky upper contact to the breccia.

Figure 3: Schematic log showing a typical section through the pyroclastic flow deposit, with a basal breccia lithofacies and upper massive lithofacies (modified after Gernon et al., 2009). Grey regions represent degassing structures. See text for details.

Figure 4: Histograms of lithic size distributions: (a) in a selection of three degassing structures (grey, superimposed) and their host matrices (black); (b) in one section of the upper massive lithofacies, and (c) in two sections of the basal layer. The lower size cut-off at -5.0 ϕ of (b) and (c: P15-P16) is due to poor sample quality (highly altered).

Figure 5: Field photograph of a typical section of the upper massive lithofacies (looking east), showing the lack of layering, scattered nature of lithic clasts, and presence of narrow degassing structures (labelled 1–4). Note the localisation of these structures around lithic clasts in the host massive lithofacies.

Figure 6: Montage of the studied unit along bench exposure X—Y (see Fig. 1), depicting particle distributions, locations of degassing structures (grey, labelled P1–P17) and rose diagrams of clast long axis orientations at corresponding reference points. All clasts are illustrated to scale. The rose diagrams were extracted from photographs of sub-vertical outcrop faces, and all rose diagrams are oriented with "up" indicating vertically up. In rose plots, pipe fabrics (transparent grey) are superimposed on host matrix fabrics (black). For all plots, the measurement interval (i.e. petal size) is 10°.

Figure 7: Degassing structures: (A) Section of drill-core showing a degassing structure localised around lithic clasts (LC); arrow indicates way-up. (B) Field

818 photograph showing two internally massive coalescing structures containing
819 angular country rock clasts (arrow indicates way-up). (C) Polished slab show-
820 ing cross-sectional view of a typical degassing structure (Ca = calcite, S = ser-
821 pentine, SO = serpentinised olivine, Ze = zeolite). Asterisks denote mixtures
822 of calcite and zeolite, which typically occur around lithic clasts. (D) & (E)
823 SEM (backscattered electron) images of the degassing structure in C (above);
824 note the void-filling calcite and zeolite (near clasts; denoted by asterisk) and
825 intergrowths of serpentine and diopside (Di; see insets). Some serpentinised
826 olivine crystals have a thin rim containing perovskite (circled). Pyroxenes (P)
827 within the interstitial matrix were likely derived from the shattering of basalt
828 clasts.

829 Figure 8: Photograph (looking SE) showing detail of the transition between
830 the basal matrix-supported breccia lithofacies and the upper massive lithofa-
831 cies; note the presence of degassing structures P14 & P15 (inset shows detail)
832 associated with the large boulder (ignore diamond drill-hole). Rose plot show-
833 ing the size and fabric orientations of lithic clasts from the basal lithofacies
834 (refer to Fig. 6 for location). Dashed lines represent percentage of the total
835 population (N = 285) within given measurement interval.

836 Figure 9: (a) & (b) Thermal demagnetization vector plots. Solid symbols give
837 the magnetisation vector for each sample (projected on to the horizontal plane)
838 at different laboratory temperatures (in °C); open symbols give the vector
839 projected onto a vertical plane at the same laboratory temperature. (c) &
840 (d) Groupings of remanence directions shown on equal-angle stereonets. Open
841 circles are projections of a magnetisation vector into the lower hemisphere (i.e.
842 negative inclination); solid circles are projections of a magnetisation vector
843 into the upper hemisphere (i.e. positive inclination). Small square cross is
844 mean direction of data and circle around it shows the 95% confidence limit of
845 the mean (expressed as an angular radius). Star is Cretaceous palaeomagnetic
846 pole (D = 350°, I = -69°). (e) T_e estimates obtained from individual basalt
847 lithic clasts. Downward pointing arrows indicate the data point is a maximum
848 T_e estimate. Dotted lines connecting two data points indicate the range in
849 T_{emp} estimates from clasts displaying a two-component magnetisation.

850 Figure 10: Schematic cartoon showing the kimberlite pyroclastic flow, (A) as
851 it enters Orapa South and undergoes a hydraulic jump, increasing its erosive
852 ability, and (B) as it degasses on a post-eruptive basis, leading to the elutria-
853 tion of fine particles from the deposit and formation of degassing structures.

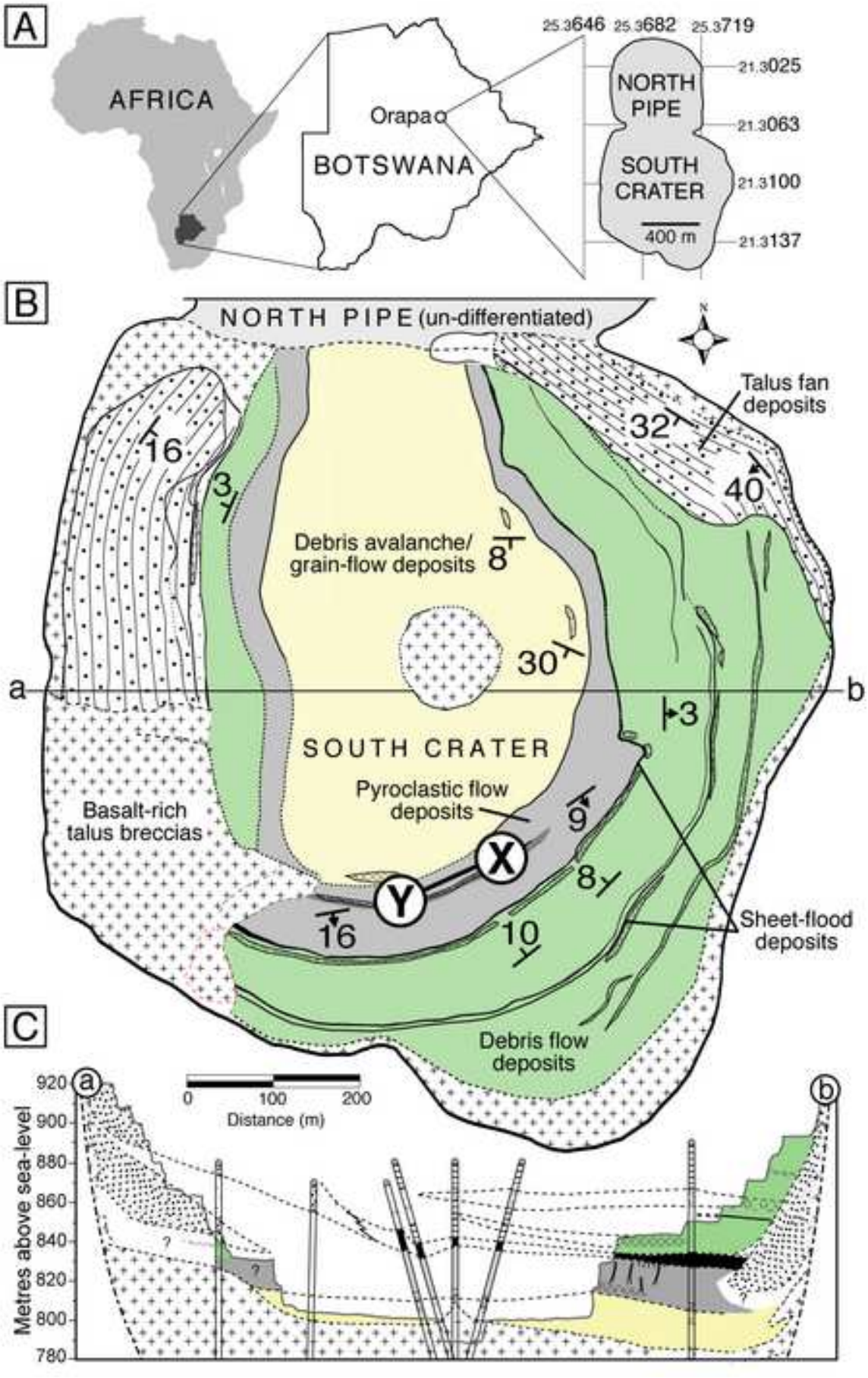

Figure 1

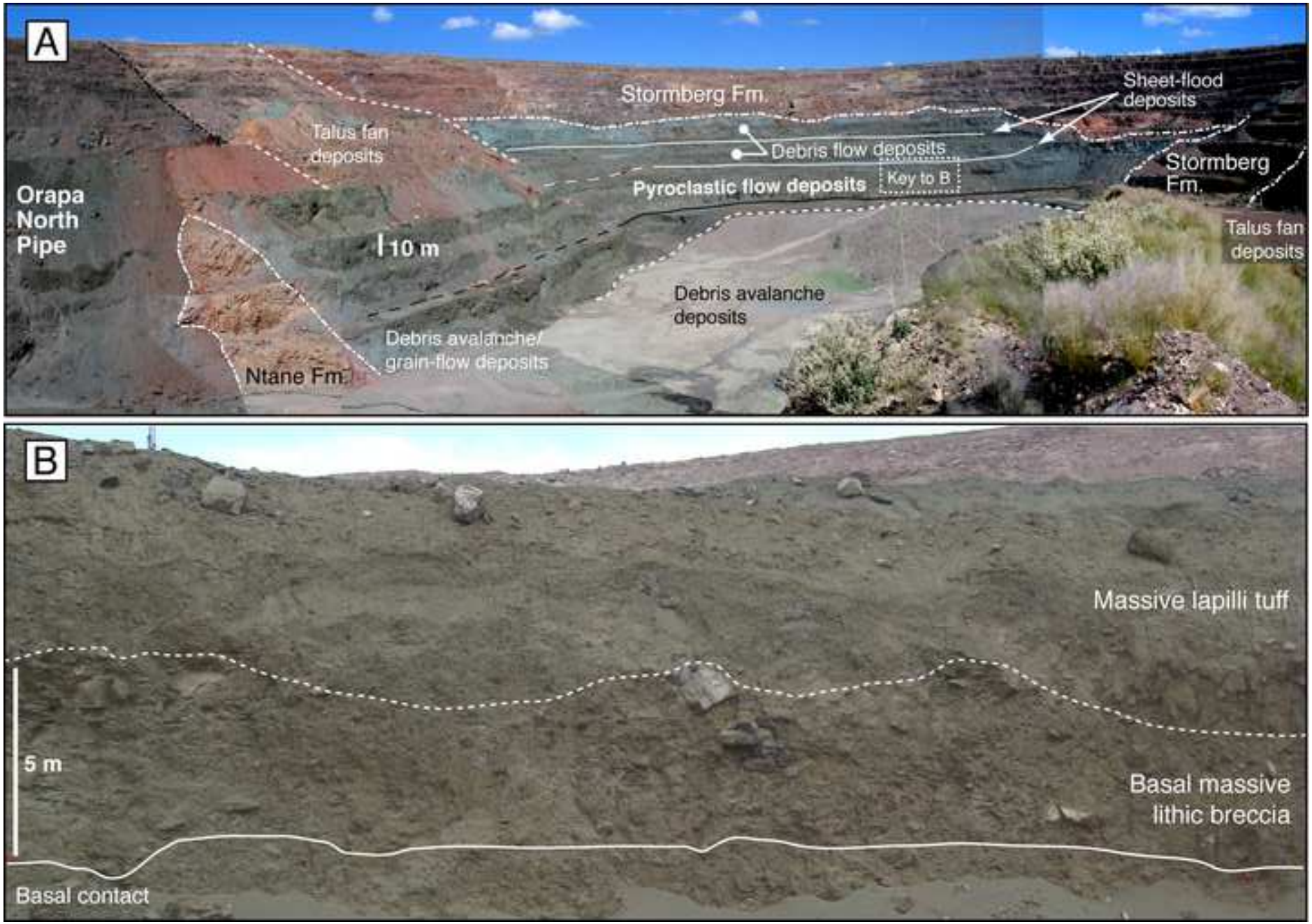

Figure 2

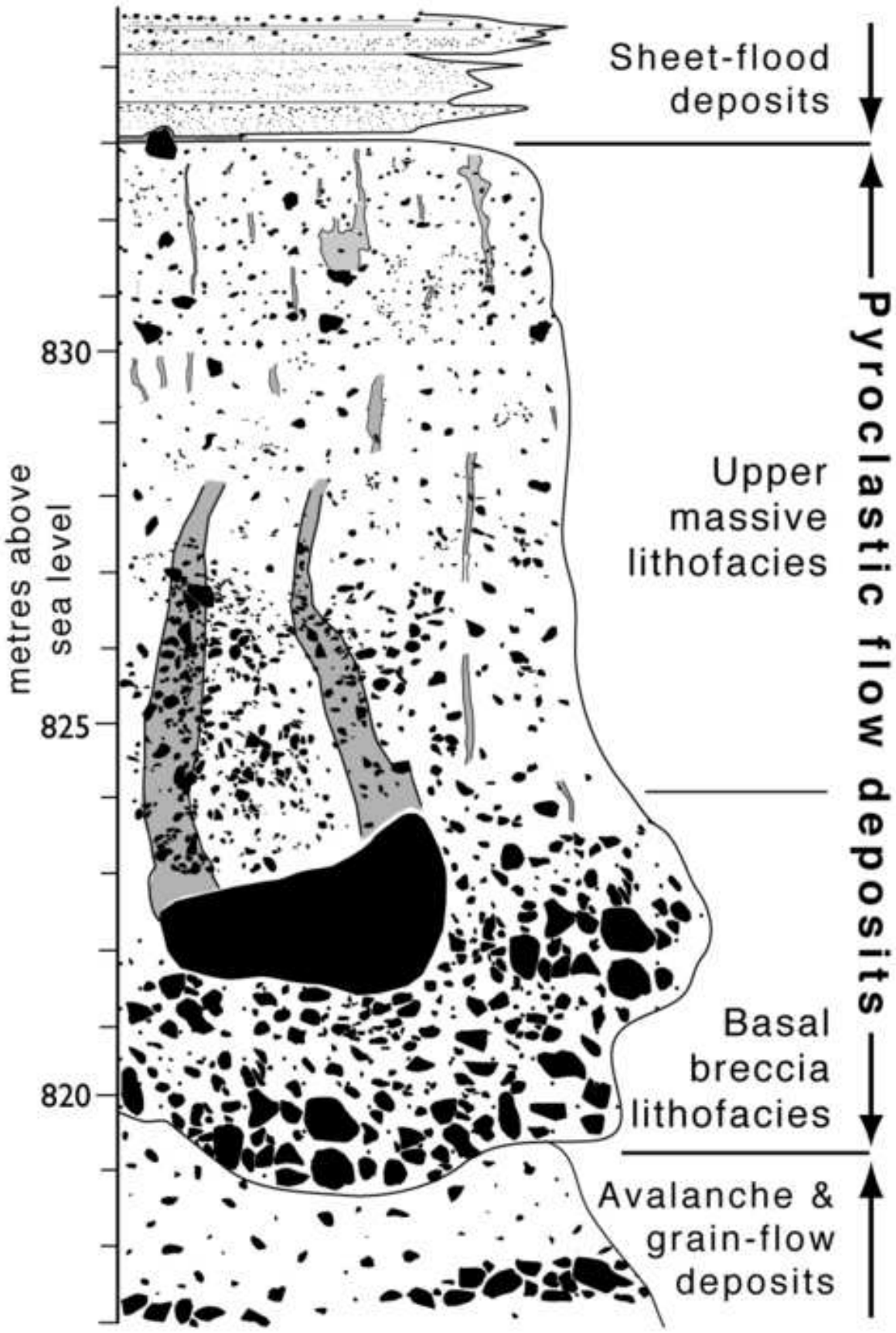

Figure 3

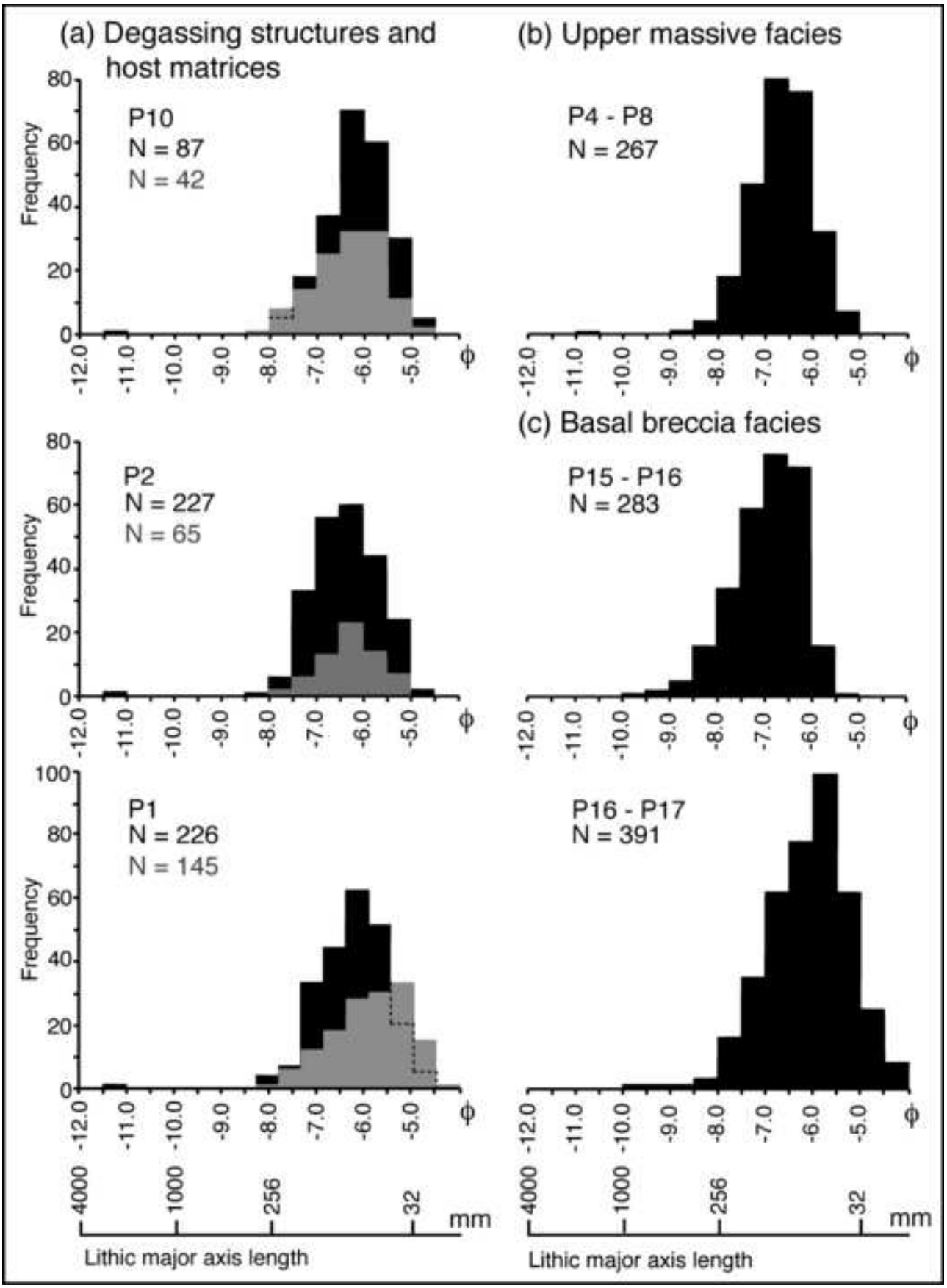

Figure 4

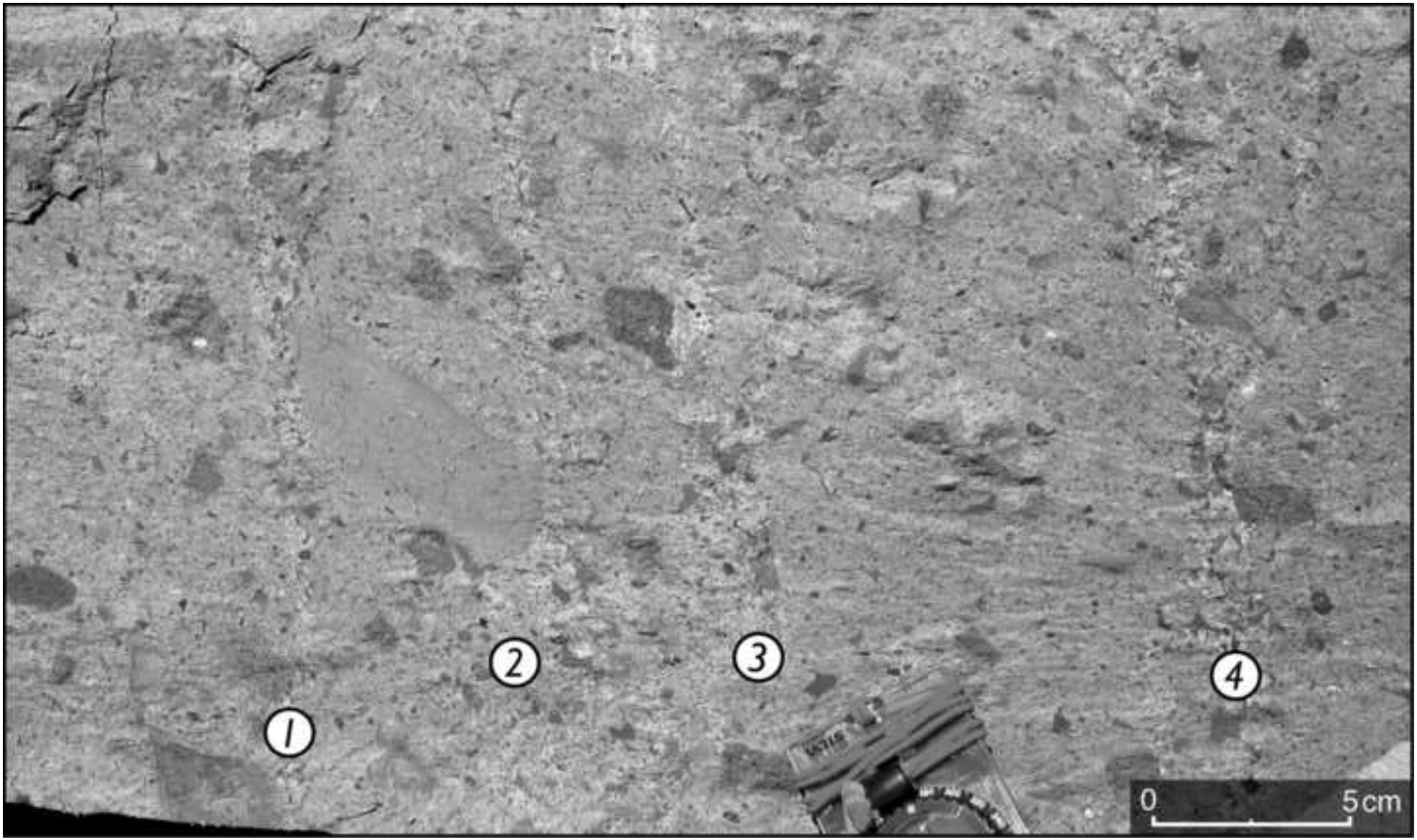

Figure 5

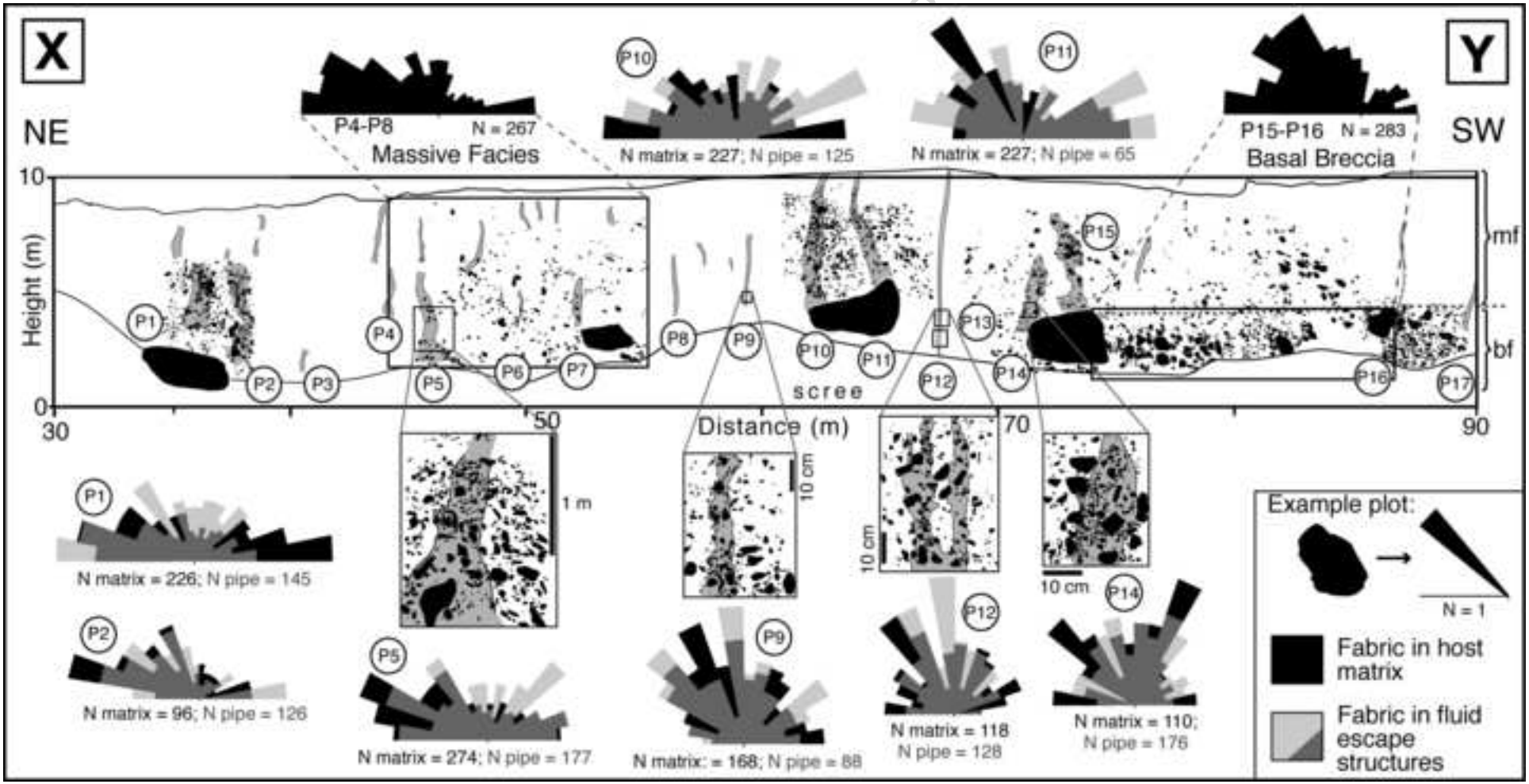

Figure 6

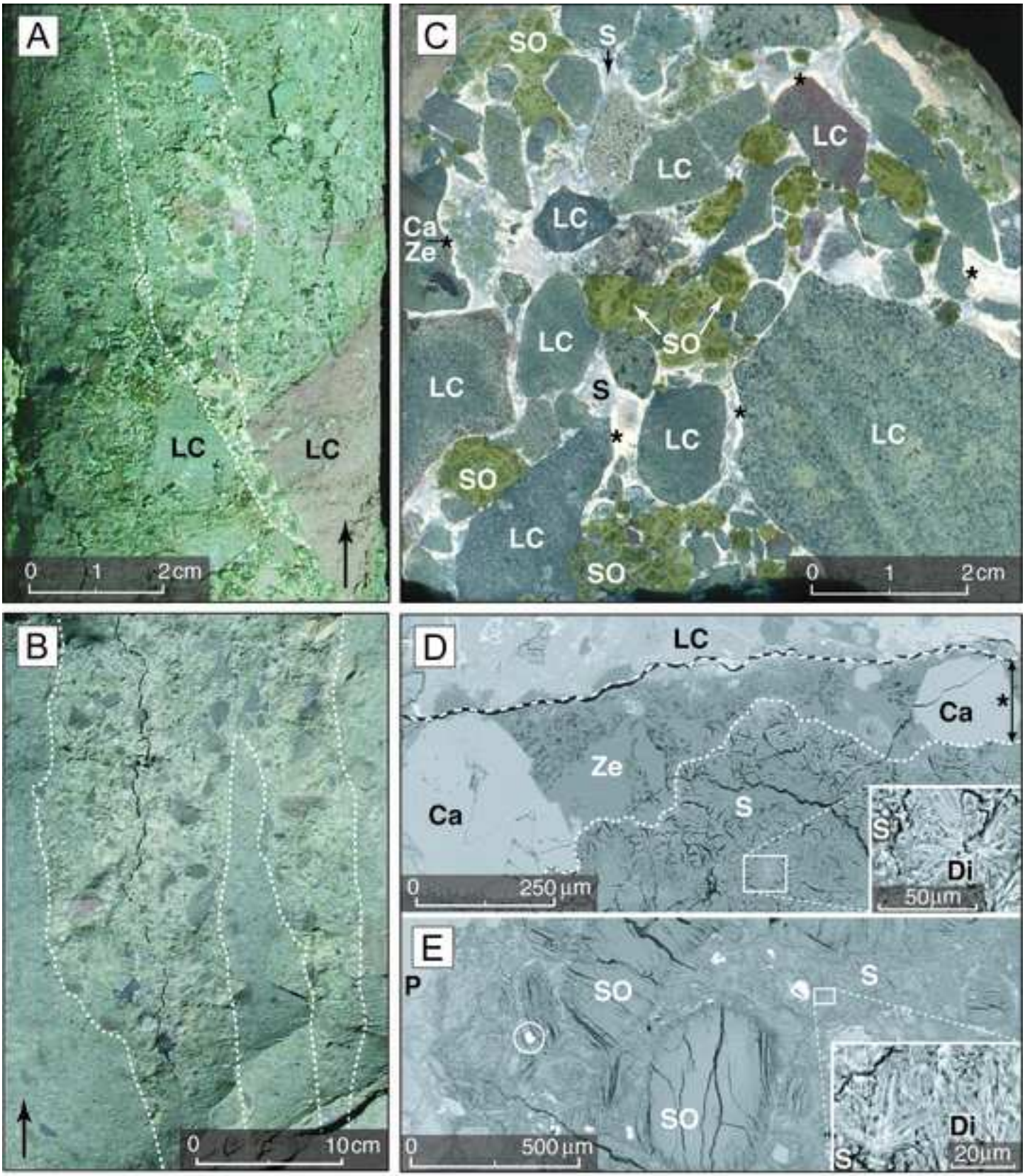

Figure 7

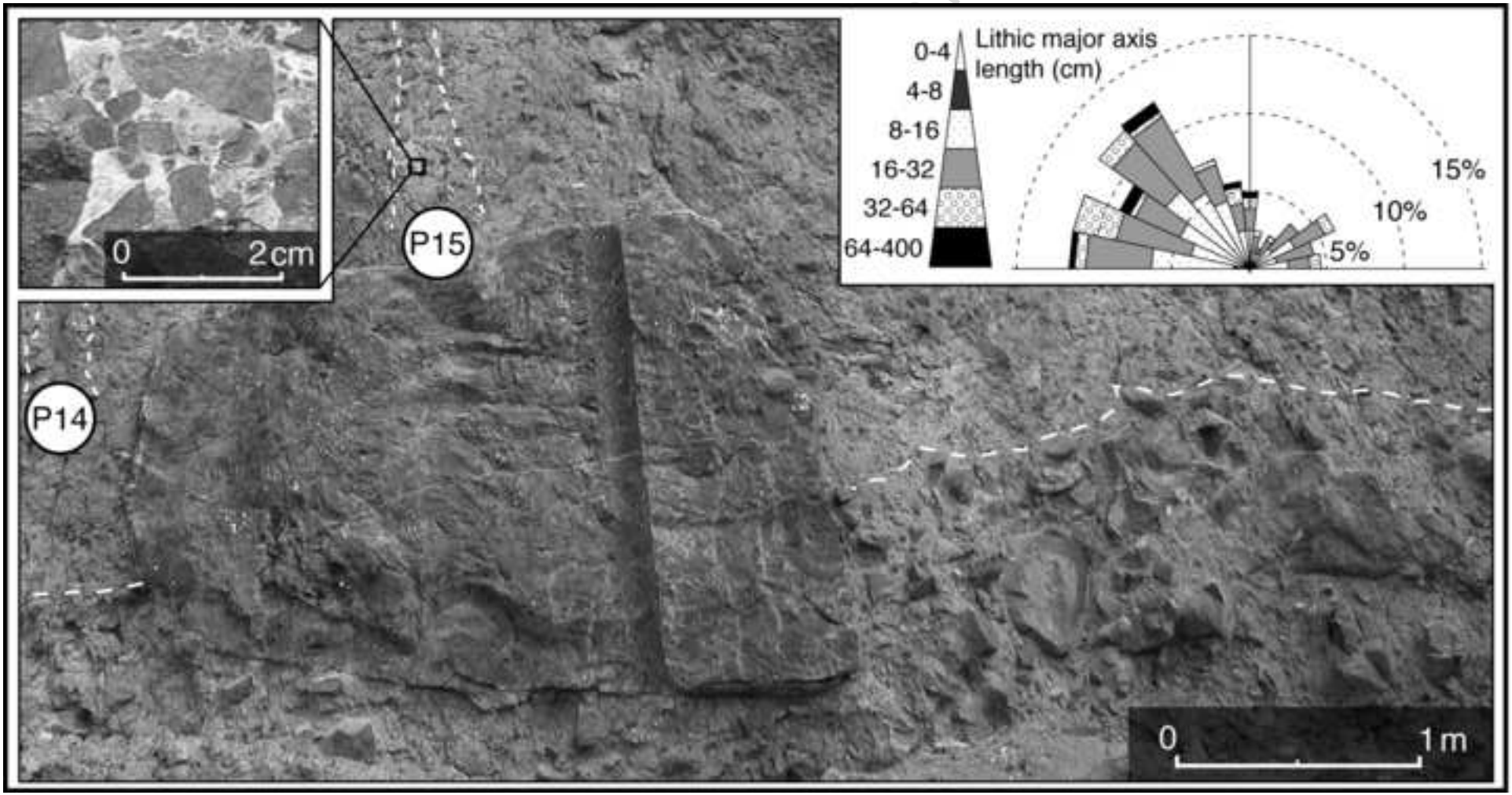

Figure 8

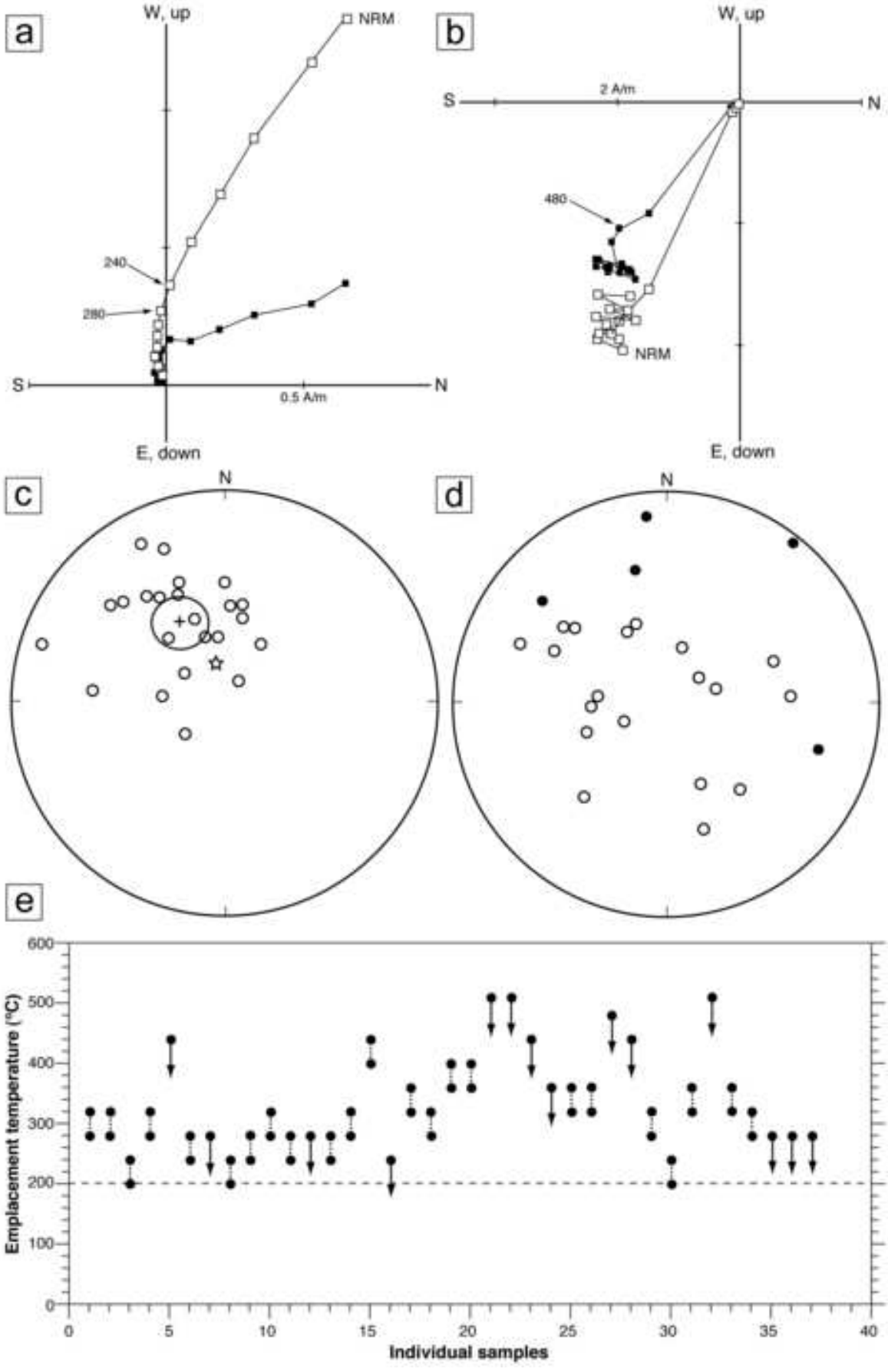

Figure 9

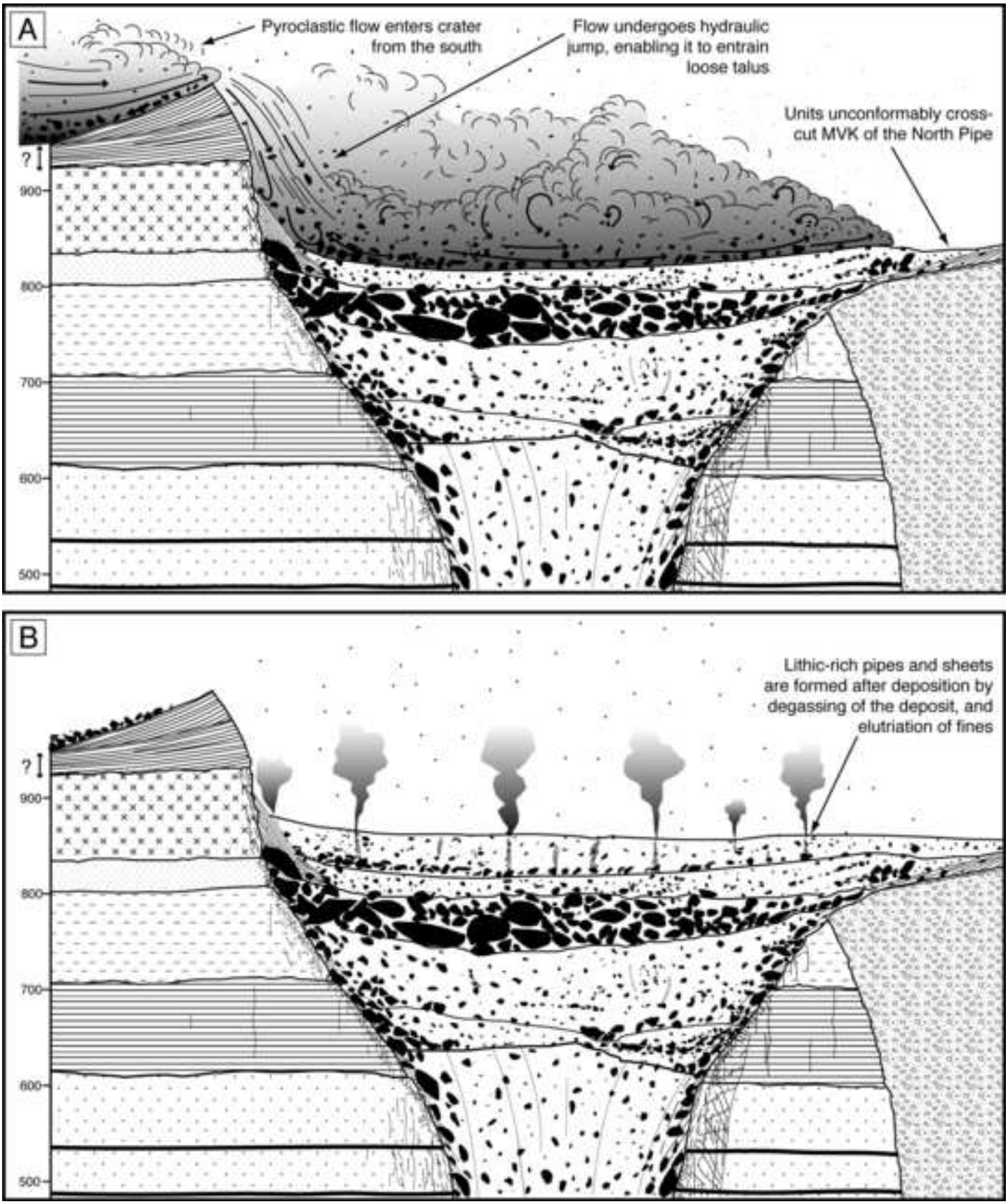

Figure 10